AD_____

Award Number: W81XWH-12-1-0284

TITLE: Development of Targeted Nanobubbles for Ultrasound Imaging and Ablation of Metastatic Prostate Cancer Lesions

PRINCIPAL INVESTIGATOR: Mohamed El-Sayed

CONTRACTING ORGANIZATION: University of Michigan
Ann Arbor, MI, 48109-2111

REPORT DATE: August 2014

TYPE OF REPORT: Annual

PREPARED FOR: U.S. Army Medical Research and Materiel Command
Fort Detrick, Maryland 21702-5012

REPORT DOCUMENTATION PAGE

Form Approved
OMB No. 0704-0188

1. REPORT DATE	2. REPORT TYPE	3. DATES COVERED
August 2014	Annual	15 Jul 2013- 14 Jul 2014

4. TITLE AND SUBTITLE
Development of Targeted Nanobubbles for Ultrasound Imaging and Ablation of Metastatic Prostate Cancer Lesions

5a. CONTRACT NUMBER

5b. GRANT NUMBER
W81XWH-12-1-0284

5c. PROGRAM ELEMENT NUMBER

6. AUTHOR(S)
Mohamed E.H. El-Sayed

E-Mail: melsayed@umich.edu

5d. PROJECT NUMBER

5e. TASK NUMBER

5f. WORK UNIT NUMBER

7. PERFORMING ORGANIZATION NAME(S) AND ADDRESS(ES)
University of Michigan
1101 Beal Avenue
Lurie Biomedical Engineering building
Ann arbor, MI, 48109-2111

8. PERFORMING ORGANIZATION REPORT NUMBER

9. SPONSORING / MONITORING AGENCY NAME(S) AND ADDRESS(ES)
U.S. Army Medical Research and Materiel Command
Fort Detrick, Maryland 21702-5012

10. SPONSOR/MONITOR'S ACRONYM(S)

11. SPONSOR/MONITOR'S REPORT NUMBER(S)

12. DISTRIBUTION / AVAILABILITY STATEMENT
Approved for Public Release; Distribution Unlimited

13. SUPPLEMENTARY NOTES

14. ABSTRACT

We already reported the synthesis of the amphiphilic PEG-*b*-(PAA)-*b*-P(HDFMA-*co*-MMA) copolymers that proved to encapsulate 1%-2% v/v PFP forming nanodroplets. We showed that NDs were able to ablate neighboring RBC as a model cells In this report, we investigated NDs ablation of prostate cells as well as the effects of ultrasound frequency on the pressure required to generate histotripsy cavitation bubbles and the resulting bubble dynamics. Results demonstrated complete fractionation and removal of cancer cells exposed to nanodroplet induced bubbles. These preliminary results support our hypothesis that ND-mediated histotripsy can be used for tumor ablation.

15. SUBJECT TERMS
Nanodroplets, mechanical cell fractionation, histotripsy, lower pressure threshold

16. SECURITY CLASSIFICATION OF:			17. LIMITATION OF ABSTRACT	18. NUMBER OF PAGES	9a. NAME OF RESPONSIBLE USAMRMC
a. REPORT	b. ABSTRACT	c. THIS PAGE			
U	U	U	UU	16	16b. TELEPHONE NUMBER *(include area*

Table of Contents

Page

1. INTRODUCTION

Many tumor types exhibit characteristically permeable vasculature with average endothelial gaps typically between 200-600 nm and show poor lymphatic drainage, which is collectively known as the enhanced permeation and retention (EPR) effect [1-4]. To take advantage of the EPR effect, phase change nanodroplets have been shown to extravasate across tumor's leaky vasculature and enter the interstitial space to directly target cancer cells [5-9]. Nanodroplets encapsulate a perfluorocarbon (PFC) core that is stabilized by albumin, lipid, or polymer shells [6, 9-11]. The PFC core typically has a boiling point lower than 37°C, but nanodroplets remain in the liquid form at body temperature [6, 11, 12]. After passing through the leaky microvasculature to a tumor's interstitial space, these nanodroplets can be vaporized by ultrasound to form gas bubbles through acoustic droplet vaporization (ADV) [6, 11, 12]. Attachment of optimal targeting ligands allows nanodroplets to specifically bind to cancer cells [6, 9, 10]. Research has shown the use of nanodroplets and ADV for targeted imaging [7, 9, 10, 13, 14], drug delivery [7, 8, 10, 14], and induce cavitation to enhance ultrasound thermal therapy [15, 16].

Our group has developed a new therapy approach combining PFC-encapsulated nanodroplets with histotripsy, a non-invasive, image-guided, ultrasound ablation method [17-20]. Histotripsy uses extremely high pressure, microseconds long pulses to generate a cluster of microbubbles (bubble cloud) from pre-existing gas pockets in the tissue where the rapid expansion and collapse of the microbubbles disrupts cells [17-22]. We hypothesize that combining histotripsy with PFC-encapsulated nanodroplets will cause the ultrasound pulses to vaporize the nanodroplets delivered to the surface of the tumor nodules and form gas bubbles. Using the resulting gas bubbles as cavitation nuclei will significantly reduce the pressure threshold needed to generate and maintain the cavitation bubble cloud, which will fractionate the tumor cells until the entire tumor destroyed. The significantly reduced pressure threshold using histotripsy combined with nanodroplets should allow selective ablation of tumors, while the surrounding normal tissue without nanodroplets would have a higher threshold and be preserved from the histotripsy-induced fractionation. Further, the resulting gas bubbles can function as ultrasound contrast agents, which will allow the tumor sites to be seen on ultrasound imaging and allow the histotripsy treatment to be guided and monitored in real-time by ultrasound imaging. By employing an ultrasound transducer with a large focal zone, this technique could also achieve efficient treatment of tumors with multiple nodules.

In another study during this annual period we looked at the frequency effect on nanodroplet mediated histotripsy. In a previous study, the feasibility of this nanodroplet-mediated histotripsy approach was demonstrated in agarose tissue phantoms containing a layer of embedded red blood cells [23]. However, red blood cells fractionate at significantly lower strain than cancer cells embedded in a three dimensional extracellular matrix. As a result, this study investigates the potential of using nanodroplet-mediated histotripsy for cancer cell ablation. To do this, prostate cancer cells were cultured inside fibrin tissue phantoms that mimicked a three dimensional tissue extracellular matrix. Histotripsy pulses were then applied to the cell surface using a custom built histotripsy transducer coupled to a microscope. Results of this study are essential to establish the ability of nanodroplet-mediated histotripsy to fractionate and remove cancer cells and will lay the groundwork for future studies developing this approach for targeted tumor ablation.

In our previous study, the feasibility of using these PFP encapsulated nanodroplets for enhanced histotripsy ablation was investigated with results support our hypothesis that nanodroplets significantly decrease the histotripsy threshold to form a cavitation bubble cloud while maintaining the effectiveness of histotripsy tissue ablation. Nanodroplet-mediated histotripsy was shown capable of creating microbubble expansion and collapse as well as well-defined ablation similar to histotripsy but at significantly lower pressure. Furthermore, the potential to use this approach for simultaneous multi-focal ablation was demonstrated.
To build upon this initial study, this work aims to investigate the effects of ultrasound frequency on nanodroplet-mediated histotripsy. We hypothesize that lower frequency will offer multiple advantages for this nanodroplet ablation therapy. First, as the transducer focal zone scales with the wavelength, a low frequency transducer will yield a large focal zone, allowing histotripsy to be applied simultaneously to cover multi-nodule tumors seeded with our nanodroplets, thus increasing the treatment efficiency for

multiple tumor nodules. With the reduced threshold at the tumor nodules with nanodroplets, only tumors will be treated while preserving surrounding normal tissue. Lower frequency is also more resistant to acoustic aberration and attenuation from bone obstruction and long overlying tissue, resulting in deeper penetration depth. Finally, we hypothesize that lower frequency will decrease the cavitation threshold using nanodroplets while still facilitating the sufficient bubble expansion required to fractionate cells. These results will improve our understanding of the nanodroplet-mediated cavitation process and help guide parameter optimization for multi-focal tumor ablation using nanodroplet-mediated histotripsy.

2. BODY

Task 1. Formulation and characterization of nano-bubble contrast agents: *To develop a strategy to formulate nano-bubble contrast agents with tunable size, PFP content, and shell flexibility to obtain stable and echogenic nano-bubbles.*

A. *Formation of NDs and size distribution of the NDs* We used 2 % PFP encapsulated in PEG_{45}-*b*-PAA_{10}-*b*-P($HDFMA_8$-*co*-MMA_{21}) copolymer. Briefly, PEG_{45}-*b*-PAA_{10}-*b*-P($HDFMA_8$-*co*-MMA_{21}) copolymers were dissolved in tetrahydrofuran (THF) (0.2% w/v) and cooled down to 0°C before the addition of PFP (2% v/v) while vigorously stirring the reaction mixture. An equal amount of water was slowly added to this solution mixture to trigger micelle formation and the mixture was stirred for 1h in an ice bath. The micelles solution was transferred into a dialysis bag (MWCO of 1 KDa) and dialyzed against ice-cold 2-(*N*-morpholino) ethanesulfonic acid (MES) solution or water to remove the THF. After 12 hours of dialysis, a slightly milky solution of PFP-loaded nanodroplets was observed. The PAA block was chemically cross-linked using 2,2`-(ethylenedioxy)-bis(ethylamine) as a cross-linker via NHS/EDC coupling chemistry [24-26] to form a flexible polymer shell that stabilizes the nanodroplets but allows acoustic droplet vaporization to form microbubbles. Selection of ideal polymer composition and PFP content used in this study has been optimized in a separate investigation (***Figure 1***).

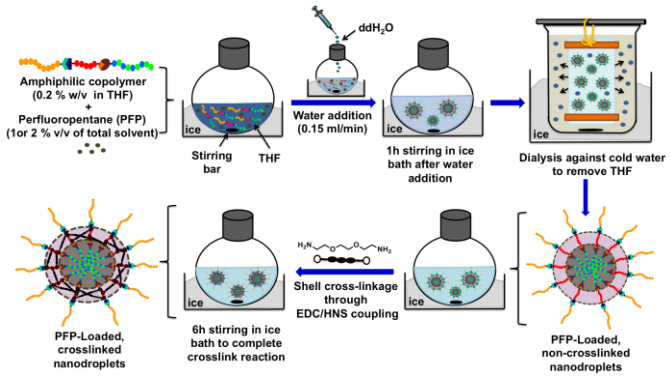

Figure 1. Self-assembly of amphiphilic copolymer into PFP-loaded nanodroplets.

We used Nanosight NS500 (NanoSight Limited, Amesbury, United Kingdom) equipped with a sample chamber with a 640nm laser and a fluoroelastomer O-ring to measure the size and concentration (i.e. number of nanodroplets/mL) of the NDs. We relied on the Nanoparticle Tracking Analysis (NTA) 2.3 software to capture and analyze images of different nanodroplets solutions and calculate the average size of each formulation **(*Figure 2*)**. Results show that the size of nanodroplets is 206±2.9-246±3.4nm at 37ºC. Our results show that nanodroplets' concentration at 22°C (3.07 x 10^{10} particles/mL) did not change upon increasing the solution temperature to 37°C (3.00 x 10^{10} particles/mL) **(*Figure 2*)**, which is critical for the success of the envisioned ablation approach as the number of cavitation nuclei is directly proportional to the number of stable nanodroplets present at tumor site. The initial testing of stability and biocompatibility of these nanodroplets is promising. Further, the size range of our nanodroplets should allow them to preferentially diffuse through the leaky tumor vasculature while preventing diffusion through normal blood vessels [1-4]. In addition, this nanodroplet design allows the covalent attachment of different targeting ligands to the free end of the PEG block allowing the incorporation of a "tunable" number of targeting motifs on the droplets surface. These targeted nanodroplets will allow selective binding to cancer cells, which will increase droplets concentration

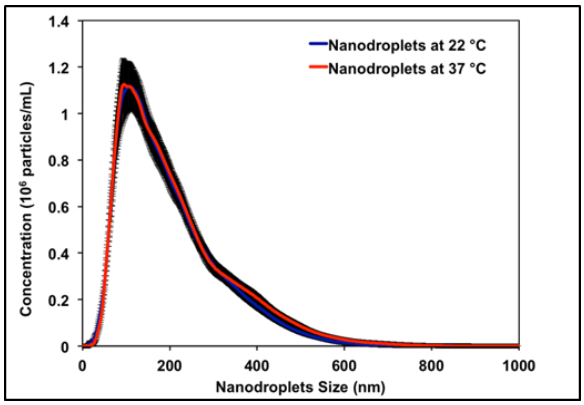

Figure 2. Nanodroplet characterization. Size distribution results show an average nanodroplet size of approximately 200 nm with a range of 95% of nanodroplets below 400 nm.

and retention in the tumor tissue. These nanodroplets are best suited for combination with histotripsy to achieve cell-specific tumor ablation.

B. Cancer Cell Phantom Preparation: To mimic a bulk tissue with cells adherent inside a 3D extracellular matrix, optically transparent fibrin-based gel phantom embedded with a layer of PC-3 and C4-2B of human prostate cancer, and MDA-MB-231 of breast cancer cell lines were used. Cells were cultured in T-Medium for C4-2B and RPMI-1640 (Invitrogen, Carllsbad, CA) with 10% fetal bovine serum (FBS; Media Tech, Manassas, VA), 1% penicillin/streptomycin (P/S; Media Tech). Cell washes were performed with sterile phosphate buffered saline (PBS; Gibco). Cells were detached for experimental seeding with 0.05% Trypsin-EDTA (Trypsin-EDTA; Cellgro). Cells were seeded inside custom built cell culture boxes (***Figure. 3***). Before cell boxes were used, they were treated in 70% ethanol and sterilized overnight under ultra violet light prior to use, then washed with PBS. Cells were seeded onto 4 mm thick fibrin gel to mimic extracellular matrix within tissue (fibrin gel was chosen for similar acoustic and mechanical properties to soft tissue). To make fibrin gel, a fibrinogen solution (Fibrinogen from bovine plasma; Sigma Aldrich) of 10 mg/ml was prepared in the culture medium without FBS or PBS, sterile filtered, and split into cell boxes. Thrombin (Thrombin; Sigma Aldrich) was then added to fibrinogen solution (80 µl of thrombin per ml fibrinogen solution). Solution was mixed and incubated at 37°C and 5% CO_2 for 1 hour prior to seeding to ensure solidification of fibrin. Cells were cultured on fibrin at least one day before histotripsy treatment. On the US treatment day 100 µL of ND formulation was added to cells and incubated for 2 h. After ND treatment left-over part of NDs were sucked out and add 50 µL of the NDs on the surface. Then, an additional 8 mm thick fibrin gel was added over NDs treated cells 1 h prior to treatment with histotripsy to mimic behavior inside a tissue (***Figure. 3***).

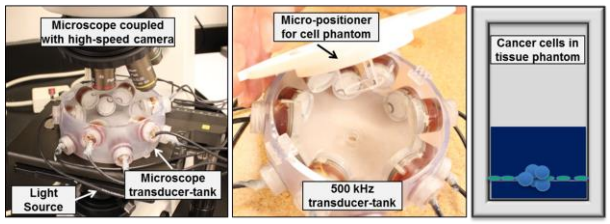

Figure 3. (A) A custom built microscope transducer-tank with a three-axis positioning system was built to investigate the ability of nanodroplet-mediated histotripsy to fractionate cancer cells. (B) Prostate cancer cells were aligned at the transducer focus using a micro-positioner, and histotripsy pulses were applied to the cancer cells which were embedded inside a fibrin gel to mimic a three dimension tissue structure (C).

C. Nanodroplet-mediated Histotripsy Cancer Cell Fractionation:

In order to study bubble-cell interactions over multiple pulses, a high-speed, 1 megapixel CCD camera (Phantom V210, Vision Research) with frame rate of 2000 fps was aligned above the microscope. Camera was externally triggered from the FPGA signal board to synchronize recorded images with the histotripsy pulse at specific delay intervals. Prostate cancer cells were cultured on fibrin gels for 3 days at 37°C and 5% CO_2 followed by treatment of cells with 100 histotripsy pulses applied at a PRF of 1 Hz. The camera was externally triggered from the FPGA board with each ultrasound pulse. The camera recorded 20 images after each pulse. In approximately 3 of these images, the bubble cloud was still present. For the remaining images, the cell displacement and deformation was observed since these effects lasted significantly longer than the bubble cloud. Microscope images were taken with a 4x magnification lens. Histotripsy pulses were applied to the cell layer with the bubble cloud and resulting cell fractionation directly observed and recorded by high-speed optical imaging after each pulse (***Figure. 4***). Nanodroplet-mediated histotripsy resulted in consistent, well-defined fractionation of cancer cells in the region in which cavitation bubbles were observed (***Figure. 4***). The cancer cell fractionation shown in ***Figure 4*** was similar to that seen with histotripsy alone, but at a pressure level well below the histotripsy intrinsic threshold. At the same applied pressure, no cavitation

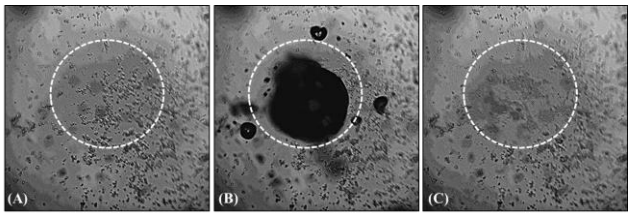

Figure 4. Preliminary cell-bubble results demonstrate nanodroplet-mediated histotripsy can fractionate prostate cancer cells into accellular debris. (A) Prostate cancer cells were cultured inside a fibrin tissue phantom to mimic cells inside a tissue extracellular matrix. 50 Histotripsy pulses were applied to the call layer containing nanodroplets at a pressure significantly below the histotripsy threshold without nanodroplets. (B) During treatment, cavitation bubbles were observed at the transducer focus and cells were observed to be mechanically ruptured. (C) After treatment, no cells

bubbles or cellular damage were observed in the samples without nanodroplets. These results are important to show that nanodroplet-mediated cavitation can indeed create cell disruption and complete fractionation of cancer cells with the same effectiveness as using histotripsy alone but at a significantly lower pressure. This is an important validation of our hypothesis confirming that the cavitating microbubbles generated via nanodroplets are destructive to use for tumor ablation. If we can perform such treatment to multi-tumor nodules simultaneously with a large focal zone transducer, the treatment efficiency is expected to be greatly improved.

D. Threshold Simulation: Effects of ultrasound frequency and initial bubble size Agarose phantoms were used to provide a well-controlled viscoelastic medium for this study, as histotripsy-induced damage is highly dependent on the tissue mechanical properties. Tissue phantoms containing 1% agarose w/v were prepared by slowly mixing In a previous histotripsy study, the threshold to generate cavitation using a single, µs-length pulse in multiple tissues and tissue-mimicking media was measured to be 26–30 MPa peak negative pressure [21]. At the high pressure above 26 MPa, cavitation bubbles are generated from pre-existing gas pockets in the tissue <10 nm in size and expanded to >50 µm followed by energetic collapse, all within a hundred µs. This energetic bubble activity disrupts adjacent cells and eventually produces complete fractionation of cells in the target tissue into a liquefied homogenate. To determine the effects of nanodroplets on reducing the peak negative pressure (*P*-) threshold to generate and expand microbubbles to >20 µm, a numerical simulation based on a modified Keller-Miksis equation for soft-tissue bubble dynamics as outlined in a previous study [21] was performed using initial gas bubbles 5–100 nm in diameter. We will refer to this threshold as the "histotripsy threshold" in this paper to distinguish from cavitation threshold commonly referred in the literature, which is often observed to be at much lower pressure levels with the presence of nuclei on the order of microns and/or using much longer pulses [27, 28]. The simulation used a 2-cycle pulse and compared frequencies of 345 kHz, 500 kHz, 1.5 MHz, and 3 MHz. The simulation showed that the histotripsy threshold decreased with decreasing frequency, especially at lower frequency **(Figure. 5)**. Nanodroplet vaporization was not accounted for in this simulation, but *P*- thresholds are expected to be sufficiently high to vaporize the nanodroplets based on the literature [6, 11].

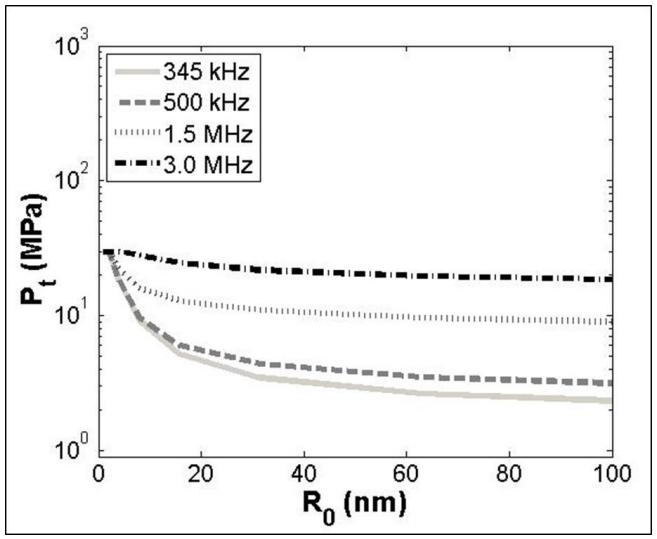

Figure 5. A plot showing the simulated peak negative pressure (P-) threshold to expand a bubble from an initial diameter of 5–100 nm to 20 µm in tissue.

E. Preparation of Agarose Phantoms: Agarose phantoms were used to provide a well-controlled viscoelastic medium for this study, as histotripsy-induced damage is highly dependent on the tissue mechanical properties. Tissue phantoms containing 1% agarose w/v were prepared by slowly mixing agarose powder (Agarose Type VII, Sigma-Aldrich, St. Louis, MO) into s saline solution (0.9% sodium chloride, Hospira) heated to above 70°C while stirring until the gel became completely transparent. Agarose solutions were degassed under a partial vacuum of 20.5 mmHg for 30 minutes before allowing the agarose solutions to cool down to 37°C. Phantoms containing nanodroplets were prepared by slowly adding the nanodoplets (2.36×10^8 particles/mL) into the agarose solution while stirring. The agarose mixtures were poured into rectangular polycarbonate holders and placed in a refrigerator at 4°C to allow the solution to solidify forming tissue phantoms with embedded nandroplets (test) or without nanodroplets (control). The Young's modulus of the tissue phantom was 38kPa [29], which is within the range of the Young's modulus of hepatocellular carcinoma tumors (20.4–75 kPa), metastatic liver tumors (23.6–75 kPa), and prostate tumors (24 kPa) [16, 30]. Tissue phantoms were warmed prior to use and maintained at 37°C for the duration of all experiments performed in this work..

F. Histotripsy Pulse Generation: Histotripsy pulses were generated at four different ultrasound frequencies (345 kHz, 500 kHz, 1.5 MHz, and 3 MHz) using three custom-built histotripsy transducers developed in house. The 345 kHz histotripsy pulses were generated by a twenty element array transducer. Each element consisted of two 690 kHz, 50-mm-diameter piezoceramic discs (SM111, Steiner and Martins, Miami, FL, USA) stacked together with epoxy, and individually mounted to a stereo-lithography-printed acoustic lens with a geometric focus of 150 mm (material: Accura® 60, 3D Systems, Rock Hill, SC, USA). The elements were confocally aligned and arranged into two rings: 1) 1st ring – eight elements with a 38-degree tilt angle, and 2) 2nd ring – twelve elements with a 62-degree tilt angle. The corresponding f-number of the 345 kHz array transducer was 0.55. The 1.5 MHz histotripsy pulses were generated using a six element array transducer. Each 1.5 MHz element consisted of a 22.5 × 22.5 mm piezoceramic square plate (SM111, Steiner and Martins). The aperture for this transducer was 79 mm in the elevational direction and 69 mm in the lateral direction with effective f-numbers of 0.7 and 0.8 in the elevational and lateral directions, respectively. The 500 kHz and 3 MHz pulses were generated by a dual frequency array transducer that consisted of twelve 500-kHz elements and seven 3-MHz elements. Each 500-kHz element consisted of two 1-MHz 20-mm-diameter piezoceramic discs (PZ36, Ferroperm, Kvistgaard, Denmark) stacked together with epoxy; each 3-MHz element consisted of a single 3-MHz, 20-mm-diameter piezoceramic disc (SM111, Steiner and Martins, Miami, FL). Both 500-kHz and 3-MHz elements were individually mounted to acoustic lenses with a geometric focus of 40 mm. The elements were confocally aligned and arranged in the following order: 1) the very bottom of the array transducer, one 3-MHz element; 2) first ring from the bottom, six 500-kHz elements with a 37° tilt angle; 3) second ring from the bottom, six 500-kHz elements with a 64° tilt angle, and 4) third ring from the bottom, six 3-MHz elements with an 85° tilt angle. Note that the 19-element dual-frequency transducer actually had four additional elements above its third ring with 103° tilt angle, but they were never used in this study.

To generate short therapy pulses, a custom high-voltage pulser developed in-house was used to drive the transducers. The pulser was connected to a field-programmable gate array (FPGA) development board (Altera DE1 Terasic Technology, Dover, DE) specifically programmed for histotripsy therapy pulsing. This setup allowed the transducers to output short pulses consisting of less than two cycles. This very short pulse minimized the possibility of cavitation occurring through shock scattering, therefore cavitation would be generated only by the negative-pressure half cycle of the incident wave. A fiber-optic probe hydrophone (FOPH) built in-house [31] was used to measure the acoustic output pressure of the transducers. At higher pressure levels, the acoustic output couldn't be directly measured due to cavitation at the fiber tip. These pressures were estimated by a summation of the output focal P-values from individual transducer elements. In a previous study [21], this estimate had a good agreement with the *P*- measured directly in a higher cavitation threshold medium, 1,3 butanediol. Sample acoustic waveforms produced by the four frequency transducers are shown in **Figure 6**.

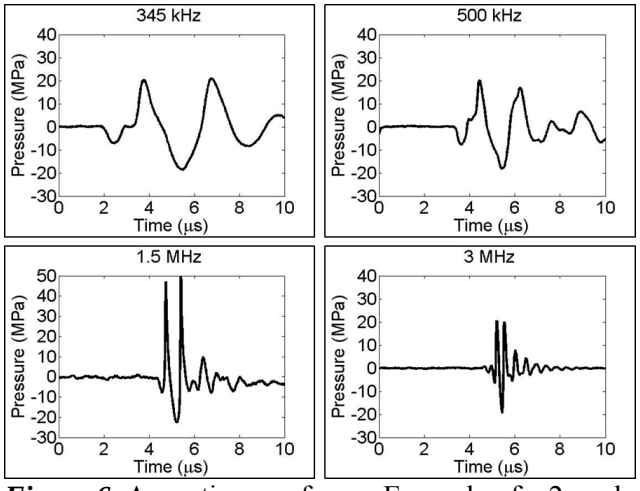

Figure 6. Acoustic waveforms. Example of a 2-cycle histotripsy pulses generated by the 345 kHz, 500 kHz, 1.5 MHz, and 3 MHz histotripsy transducers.

For cavitation threshold and bubble expansion experiments, histotripsy pulses were applied inside different samples at a pulse repetition frequency (PRF) of 0.5 Hz. The PRF was kept very low to minimize the possibility that cavitation from 1 pulse would change the probability of cavitation on a subsequent pulse. In a previous study, it was demonstrated that for PRFs > 1 Hz, cavitation during a pulse increased the likelihood of cavitation on a following pulse, but this effect was not observed for PRFs below 1Hz [21]. In solid samples, the focus was translated for each pulse by 1 mm transverse to the acoustic propagation direction in a 10 × 10 grid for each pressure level in order to minimize the effects of cavitation damage to the solid sample resulting from altering the probability of cavitation. Each focal volume in the sample

received no more than one pulse at each acoustic pressure level, and only in a fraction of these did cavitation occur. At each pressure level tested, 100 pulses were applied to the sample.

G. Optical Imaging, Image Processing, PCD Measurements and Signal Processing: High speed optical imaging was used to capture images of the focal zone after the propagation of each pulse through the focus for water and agarose tissue phantoms using two high speed cameras (**Figure. 7**). For experiments with the 345 kHz and 1.5 MHz transducers, a high-speed, 1 megapixel CCD camera (Phantom V210, Vision Research) was aligned with the transducer and backlit by a continuous light source. The camera was focused using a macro-bellows lens (Tominon, Kyocera), giving the captured images a resolution of approximately 5.9 µm per pixel and 3.4 µm per pixel for 345 kHz and 1.5 MHz, respectively. For experiments with the 500 kHz and 3 MHz dual frequency transducer, a digital, 1.3-megapixel CCD camera (PN: FL3-U3-13Y3M-C, Flea® 3, PointGrey, Richmond, BC, Canada) was positioned perpendicularly to the dual-frequency array transducer facing one of its optical windows. A Nikon 4X objective was attached to the camera with extension tubes to magnify the image plane, giving the captured images a resolution of approximately 2.5 µm per pixel. A pulsed white-light LED was placed on the diametrically-opposed optical window of the dual-frequency array transducer, which provided back-lit illumination.

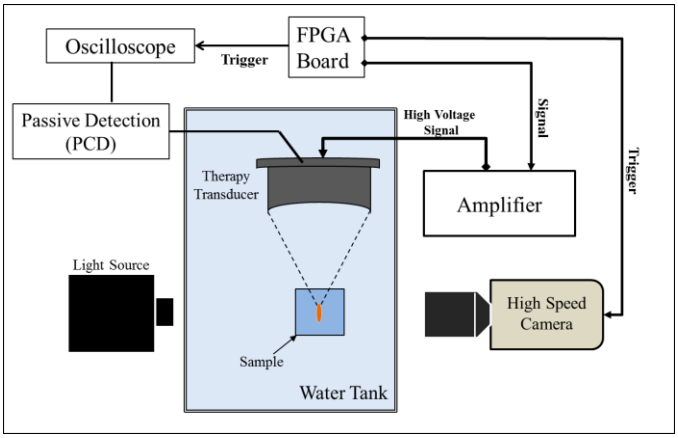

Figure7. Experimental set-up. The focus of the histotripsy transducer was aligned inside tissue phantoms containing nanodroplets. Cavitation was monitored using high speed optical imaging and passive cavitation detection using one of the therapy elements.

The cameras were triggered to record one image for each applied pulse. After acquisition, shadowgraph images were converted from grayscale to binary by an intensity threshold determined by the background intensity using image processing software (MATLAB, The Mathworks). Bubbles were indicated as any black regions >5 pixels. The minimum resolvable bubble radius was <15 µm for all frequencies due to the magnification of the described experimental arrangement and minimum 5-pixel area. For threshold experiments, the number of frames that contained detected cavitation bubbles on an image was recorded, and the fraction of total frames for which any cavitation was detected was determined as the cavitation probability. High speed imaging simplifies the detection of cavitation in transparent media but could not be used with tissue samples. As a result, an acoustic method was also used to identify cavitation in the focal zone in all media. For each experiment, one of the transducer's therapy elements was also used as a passive cavitation detector (PCD) to detect for the presence of bubbles in the focal region (**Figure 7**). The PCD element signal was connected to an oscilloscope (LT372; Lecroy, Chestnut Ridge, NY, USA) with the time window selected to record the backscatter of the pressure pulse from cavitation bubbles [21, 32, 33].

To determine whether cavitation occurred during a pulse, the signal generated by backscattering of the incident pulse from the focus was analyzed following the method used in the previous study by Maxwell et al [21]. A significant fraction of the incident wave energy is scattered when a cavitation bubble expands, greatly increasing the backscattered pressure amplitude received by the PCD. This signal appeared on the PCD at the time point corresponding to two times the time of flight for the focal length of the respective transducers. The integrated frequency power spectrum (S_{PCD}) of the backscatter signal was used as a measure of whether cavitation occurred during the pulse according to the method previously described in the paper by Maxwell et al [21]. This method allowed a quantitative definition of whether a signal was above the threshold for cavitation, based on whether the backscattered signal was much larger than the baseline values when cavitation was not observed. Using this PCD method, the results gave good agreement with the optical imaging method for all transparent samples tested in this study.

H. Measurement of Histotripsy Threshold in Agarose Tissue Phantoms: T In order to validate the cavitation threshold simulation results, the pressure threshold was measured in tissue-mimicking agarose phantoms with and without nanodroplets. For all frequency histotripsy pulses applied to agarose tissue phantoms, cavitation bubbles were observed on the high-speed camera in an increasingly larger area with increasing pressure when a certain negative pressure was exceeded. **Figure 8** shows example images taken for 1.5 MHz experiments (**Figure 8**). The probability of observing cavitation in the focal volume followed a sigmoid function, given by $P(p_-) = \frac{1}{2} + erf\left(\frac{p_- - p_t}{\sqrt{2\sigma^2}}\right)$, where *erf* is the error function, p_t is the pressure at which the probability $P_{cav} = 0.5$, σ is a variable related to the width of the transition between $P_{cav} = 0$ and $P_{cav} = 1$, with $\pm\ \sigma$ giving the difference in pressure from about $P_{cav} = 0.15$ to $P_{cav} = 0.85$ for the fit [21]. Curve fitting for all data sets was performed using an OriginLab curve fitting program (OriginLab Corporation, Northampton, MA). In addition to high speed imaging, cavitation was monitored using one of the therapy transducers for passive cavitation detection following a previously established method [21]. The PCD detected a distinct signal in the presence of single or multiple cavitation events. First, a multi-cycle burst with a center frequency near the therapy transducer frequency was detected with a time delay corresponding to twice the time for the therapy pulse to travel from the transducer to the focus. When no cavitation was observed on high-speed camera, the scattered signal was small (**Figure 8**). The accuracy of detection was validated in the set of data for water. Figure 7 shows an example of the relative values of S_{PCD} versus pulse number for 100 pulses near the cavitation pressure threshold p_t in degassed, distilled water using the 1.5 MHz transducer (**Figure 9**). The values for P_t in agarose phantoms without nanodroplets were found to be between $P_t = 24.8 \pm 1.1$ MPa for 345 kHz, $P_t = 25.5 \pm 1.74$ MPa for 500 kHz, $P_t = 26.7 \pm 0.36$ MPa for 1.5 MHz, and $P_t = 26.8 \pm 0.46$ MPa for 3 MHz (**Figure 10 Table 1**). Note that at lower amplitudes, cavitation was occasionally observed that deviated from the curve function. These cavitation events were probably caused by contamination of the sample by heterogeneities in the liquid that could not be entirely avoided throughout the experiment. In the experimental data for all frequencies, cavitation was observed with $P_{cav} = 1$ for $p_- > -30$ MPa. As P_{cav} approached 1, multiple cavitation bubbles were observed by high-speed imaging of each pulse within the focal region. As pressure was increased above P_t, the bubbles were visualized in an increasingly larger area with a greater number of bubbles present in this focal region as has been previously observed [21, 34]. Although the bubbles covered a larger area at higher pressure, the diameter of individual bubbles appeared to be consistent between pulses and at different pressure levels at the time point captured by the camera. However, differences in bubble size were noticed for different frequencies with lower frequency producing larger bubbles.

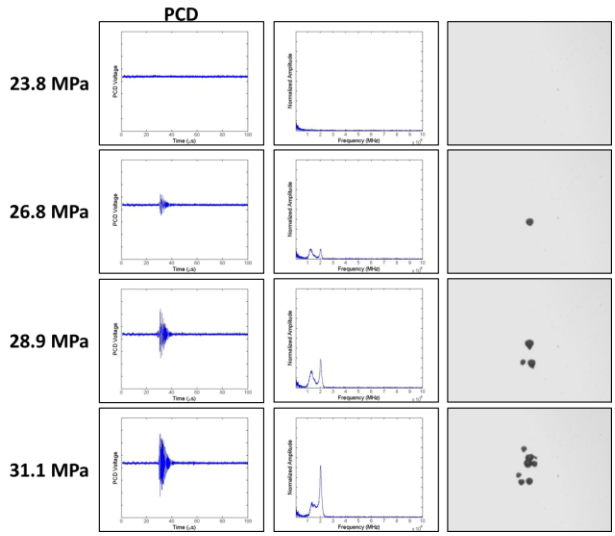

Figure 8. Cavitation Detection. Sample PCD temporal (left) and frequency (center) signals were used for cavitation detection. Results showed agreement with high speed optical images of cavitation (right). Representative images shown are from 1.5 MHz histotripsy pulses applied to degassed water.

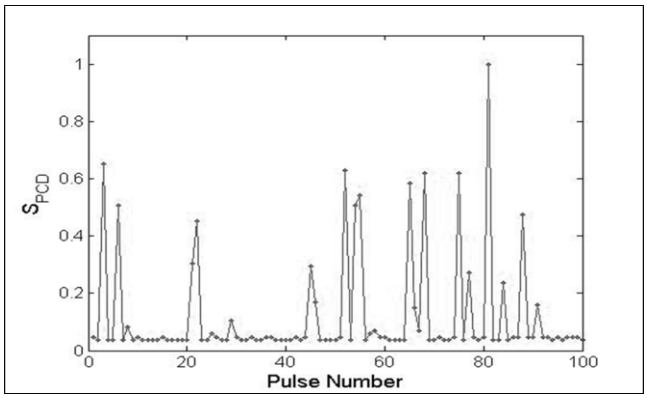

Figure 9. Example of Integrated Power Spectrum (SPCD) Bimodal distribution. Result show the SPCD for 100 histotripsy pulses applied by the 1.5 MHz transducer at a peak negative pressure of 25.3 MPa. A bimodal distribution is evident, with the lower, more consistent values indicating the absence of cavitation, and the larger, more variable values indicating the presence of one or more bubbles.

The effects of nanodroplets on the cavitation threshold demonstrated a significant decrease in the cavitation threshold at lower frequency, dropping to P_t = 6.5±0.16 MPa and P_t = 10.3±0.35 MPa at 345 kHz and 500 kHz, respectively (**Figure 10, Table 1**). At 1.5 MHz, the cavitation threshold with nanodroplets only dropped slightly to P_t = 23.3±0.18 MPa (**Figure. 10, Table 1**). A larger decrease in threshold with nanodroplets was once again seen at 3 MHz, with P_t = 18.0±0.63 MPa (**Figure 10, Table 1**). The results of the cavitation threshold for all frequencies are plotted in **Figure 11**. The decrease in the cavitation threshold for samples with nanodroplets compared to the corresponding control phantoms at each frequency was 18.3 MPa, 15.2 MPa, 2.4 MPa, and 8.8 MPa at 345 KHz, 500 kHz, 1.5 MHz, and 3 MHz, respectively. These results suggest that a lower frequency would be better suited to use for nanodroplet-mediated histotripsy, as it results in a significantly lower histotripsy threshold. This dependence is opposite to a previous study by Kripfgans et al. using micron-sized droplets, where they found the pressure threshold to vaporize the droplets decreased with increasing frequency [12]. In comparison, we used much smaller droplets and measured the threshold to expand the bubbles resulting from vaporized droplets to >50μm. It is likely that a different mechanism is responsible for our study, which is suggested by the fact that the trend of increasing threshold with increasing frequency didn't continue at 3 MHz. It is possible that the trend of decreasing threshold with decreasing frequency, which is consistent with the frequency dependency in inertial cavitation, only occurs when the cavitation threshold inside the droplet is below the ADV threshold. Future experiments will investigate the role of these two potential mechanisms in nanodroplet-mediate histotripsy.

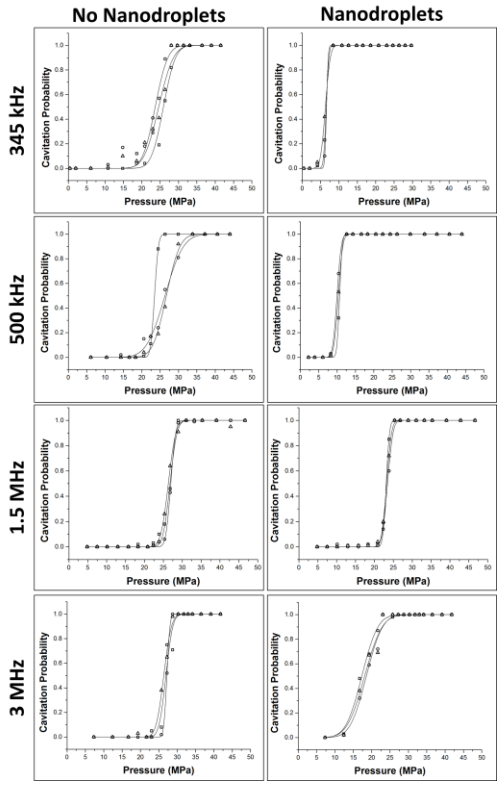

Figure 10. Cavitation threshold in tissue phantoms with and without nanodroplets. Example probability curves for mechanically tunable agarose tissue phantoms. Results showed no significant difference in the intrinsic threshold as with increasing stiffness. A small increase of ~2-3 MPa was observed in

I. Bubble Behavior: The bubble expansion and collapse observed in histotripsy is substantially more energetic than traditionally defined inertial cavitation where the maximal bubble diameter becomes equal or greater than twice the initial bubble size [35]. In histotripsy, microbubbles formed from preexisting nuclei <10 nm grow to over 50 μm before violently collapsing, all occurring within 100 μs. This bubble behavior is critical to achieve cell disruption. To study the effects of ultrasound frequency on the behavior of cavitation bubbles generated by nanodroplet-mediated histotripsy, optical images of bubbles were recorded by the high-speed camera at different time delays after the arrival of histotripsy pulses produced by 345 kHz, 500 kHz, 1.5 MHz, and 3 MHz histotripsy transducers. The peak negative pressure used for each frequency was chosen to be slightly above the nanodroplet threshold at each frequency so that cavitation was always generated (P_{cav}=1). In agarose gel, the bubble radius increased to the maximum radius of 84.5±24.1 μm at 345 kHz (*P*-=10.8 MPa), 59.9±11.9 μm at 500 kHz (*P*-=14.5 MPa), 62.5±10.5 μm at 1.5 MHz (*P*-=26.8 MPa), 20.9±4.1 μm at 3 MHz (*P*-=23.0 MPa) (**Figure 12**). The level of bubble expansion at lower frequency (>50 μm) is similar to the behavior of bubbles previously observed to cause tissue ablation using histotripsy alone at higher

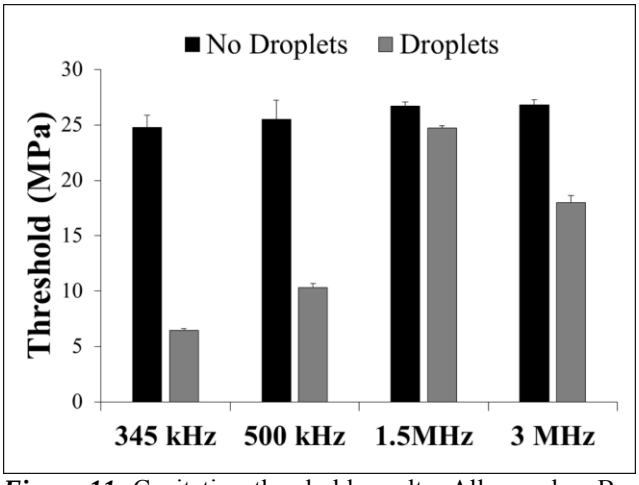

Figure 11. Cavitation threshold results: All samples. Bar plots show the cavitation threshold results for all samples and frequencies studied in this work.

pressures and is anticipated to create similar cell disruption. All these finding that we have got related to cell ablation and frequency studies are ready to submit the manuscripts to be published.

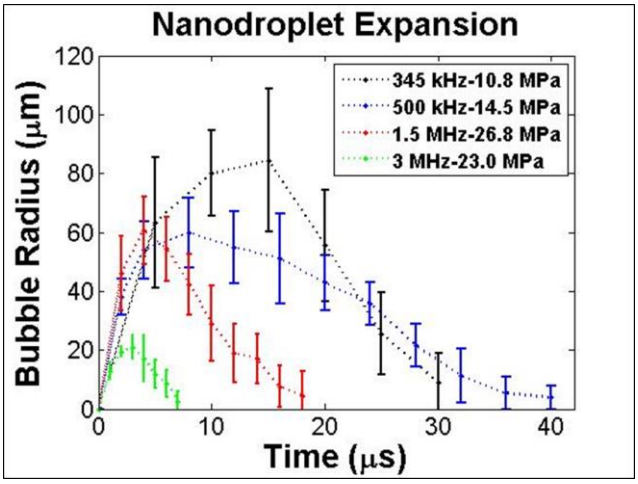

Figure 12. Bubble behavior. Radius vs. Time plots of bubbles formed from nanodroplets above the nanodroplet threshold show lower frequency facilitated larger bubble expansion despite the decrease in pressure required to generate the bubbles.

3. KEY RESEARCH ACCOMPLISHMENTS

- Nanodroplet-mediated histotripsy can create cell disruption and fractionation of cancer cells with the same effectiveness as using histotripsy alone but at a significantly lower pressure.
- Based on our previous and current studies nanodroplet-mediated histotripsy can be used for targeted, multi-focal tumor ablation.
- We can get a significantly lower pressure threshold to generate cavitation bubbles at 345 kHz and 500 kHz compared to 1.5 MHz and 3 MHz.
- The bubble expansion is enhanced at lower frequency, despite the reduced cavitation threshold.
- Lower frequency offers multiple advantages for ablation therapy including a larger focal zone which would allow nanodroplet-mediated histotripsy to be applied simultaneously to cover multi-nodule tumors seeded with our nanodroplets
- Selective ablation of PFP-Loaded nanodroplets proved that cavitation should be selectively generated in multi-tumor nodules with nanodroplets inside the focal zone, whereas no cavitation should be formed at normal tissue because of a reduced threshold at the tumor nodules with nanodroplets.
- These nanodroplets have a potential to be used as imaging agent in-vivo
- They are not toxic at the level of tested concentration.

4. REPORTABLE OUTCOMES

- Yasemin Yuksel Durmaz, Eli Vlaisavljevich, Zhen Xu, and Mohamed E.H. ElSayed, "Development of nanodroplets for histotripsy-mediated cell ablation", Molecular Pharmaceutics, 11(10): 3684–3695, 2014.
- Eli Vlaisavljevich, Yasemin Yuksel Durmaz, Adam Maxwell, Mohamed E.H. ElSayed, Zhen Xu*, "Nanodroplet-mediated histotripsy for image-guided targeted ultrasound cell ablation", Theranostics, 3(11): 802-815, 2013.
- O. Aydin, E. Vlaisavljevich, Y. Y. Durmaz, M. ElSayed1, Z. Xu, "Nanodroplet-Mediated Histotripsy Cancer Cell Ablation", Manuscript in preparation.
- E. Vlaisavljevich, O. Aydin, Y. Y. Durmaz, M. ElSayed, Z. Xu "The Effects of Ultrasound Frequency on Nanodroplet-Mediated Histotripsy" Ready to submit.

5. CONCLUSION

The findings in this work demonstrate proof of concept for cancer cell ablation using nanodroplet-mediated histotripsy. Results demonstrated that prostate cancer cells embedded inside a 3D tissue-like fibrin phantom were completely fractionated and removed from the region in which nanodroplet induced cavitation bubbles were observed. This finding suggests that nanodroplet-mediated histotripsy can create cell disruption and fractionation of cancer cells with the same effectiveness as using histotripsy alone but at a significantly lower pressure. This finding builds upon our previous study and supports the hypothesis that nanodroplet-mediated histotripsy can be used for targeted, multi-focal tumor ablation.

Furthermore, in terms of frequency studies, the effects of ultrasound frequency on nanodroplet-mediated histotripsy was investigated. Results demonstrated a significantly lower pressure threshold to generate cavitation bubbles at 345 kHz and 500 kHz compared to 1.5 MHz and 3 MHz. Furthermore, results demonstrated bubble expansion was enhanced at lower frequency, despite the reduced cavitation threshold. These results suggest that using lower frequency can significantly improve nanodroplet-mediated histotripsy. Lower frequency offers multiple advantages for ablation therapy including a larger focal zone which would allow nanodroplet-mediated histotripsy to be applied simultaneously to cover multi-nodule tumors seeded with our nanodroplets, thus increasing the treatment efficiency for multiple

tumor nodules. Furthermore, as shown in this study, a reduced threshold at the tumor nodules with nanodroplets will allow only the tumors to be treated while preserving surrounding normal tissue. Finally, lower frequency is also more resistant to acoustic aberration and attenuation from bone obstruction and long overlying tissue, resulting in deeper penetration depth. Overall, the results of this study provide significant insight in the role of ultrasound parameters on nanodroplet guided histotripsy and will provide a rational basis to specifically tailor acoustic parameters for efficient multi-focal tumor ablation.

6. References

[1] R.B. Campbell, Tumor physiology and delivery of nanopharmaceuticals, Anticancer Agents Med Chem, 6 (2006) 503-512.

[2] J. Fang, H. Nakamura, H. Maeda, The EPR effect: Unique features of tumor blood vessels for drug delivery, factors involved, and limitations and augmentation of the effect, Adv. Drug Deliv. Rev., 63 (2011) 136-151.

[3] S.K. Hobbs, W.L. Monsky, F. Yuan, W.G. Roberts, L. Griffith, V.P. Torchilin, R.K. Jain, Regulation of transport pathways in tumor vessels: role of tumor type and microenvironment, Proc Natl Acad Sci U S A, 95 (1998) 4607-4612.

[4] V. Torchilin, Tumor delivery of macromolecular drugs based on the EPR effect, Adv Drug Deliv Rev, 63 (2011) 131-135.

[5] L. Du, Y. Jin, W. Zhou, J. Zhao, Ultrasound-Triggered Drug Release and Enhanced Anticancer Effect of Doxorubicin-Loaded Poly(D,L-Lactide-Co-Glycolide)-Methoxy-Poly(Ethylene Glycol) Nanodroplets, Ultrasound Med Biol, 37 (2011) 1252-1258.

[6] Z. Gao, A.M. Kennedy, D.A. Christensen, N.Y. Rapoport, Drug-loaded nano/microbubbles for combining ultrasonography and targeted chemotherapy, Ultrasonics, 48 (2008) 260-270.

[7] N. Rapoport, K.-H. Nam, R. Gupta, Z. Gao, P. Mohan, A. Payne, N. Todd, X. Liu, T. Kim, J. Shea, C. Scaife, D.L. Parker, E.-K. Jeong, A.M. Kennedy, Ultrasound-mediated tumor imaging and nanotherapy using drug loaded, block copolymer stabilized perfluorocarbon nanoemulsions, Journal of Controlled Release, 153 (2011) 4-15.

[8] N.Y. Rapoport, A.M. Kennedy, J.E. Shea, C.L. Scaife, K.-H. Nam, Controlled and targeted tumor chemotherapy by ultrasound-activated nanoemulsions/microbubbles, Journal of Controlled Release, 138 (2009) 268-276.

[9] P.S. Sheeran, S. Luois, P.A. Dayton, T.O. Matsunaga, Formulation and acoustic studies of a new phase-shift agent for diagnostic and therapeutic ultrasound, Langmuir, 27 (2011) 10412-10420.

[10] K. Kawabata, R. Asami, T. Axuma, S. Umemura, Acoustic response of microbubbles derived from phase-change nanodroplet., Jpn J Appl Phys, (2010).

[11] P.S. Sheeran, P.A. Dayton, Phase-change contrast agents for imaging and therapy, Curr Pharm Des, 18 (2012) 2152-2165.

[12] O.D. Kripfgans, J.B. Fowlkes, D.L. Miller, O.P. Eldevik, P.L. Carson, Acoustic droplet vaporization for therapeutic and diagnostic applications, Ultrasound Med Biol, 26 (2000) 1177-1189.

[13] P.S. Sheeran, V.P. Wong, S. Luois, R.J. McFarland, W.D. Ross, S. Feingold, T.O. Matsunaga, P.A. Dayton, Decafluorobutane as a phase-change contrast agent for low-energy extravascular ultrasonic imaging, Ultrasound Med Biol, 37 (2011) 1518-1530.

[14] K. Wilson, K. Homan, S. Emelianov, Biomedical photoacoustics beyond thermal expansion using triggered nanodroplet vaporization for contrast-enhanced imaging, Nat Commun, 3 (2012) 618.

[15] J.A. Kopechek, P. Zhang, M.T. Burgess, T.M. Porter, Synthesis of phase-shift nanoemulsions with narrow size distributions for acoustic droplet vaporization and bubble-enhanced ultrasound-mediated ablation, J Vis Exp, (2012) e4308.

[16] M. Zhang, M.L. Fabiilli, K.J. Haworth, F. Padilla, S.D. Swanson, O.D. Kripfgans, P.L. Carson, J.B. Fowlkes, Acoustic droplet vaporization for enhancement of thermal ablation by high intensity focused ultrasound, Acad Radiol, 18 (2011) 1123-1132.

[17] E. Vlaisavljevich, Y. Kim, S. Allen, G. Owens, S. Pelletier, C. Cain, K. Ives, Z. Xu, Image-Guided Non-Invasive Ultrasound Liver Ablation using Histotripsy: Feasibility Study in an *In Vivo* Porcine Model. , Ultrasound Med Biol, (2013).

[18] F. Winterroth, Z. Xu, T.Y. Wang, J.E. Wilkinson, J.B. Fowlkes, W.W. Roberts, C.A. Cain, Examining and analyzing subcellular morphology of renal tissue treated by histotripsy, Ultrasound Med Biol, 37 (2011) 78-86.

[19] Z. Xu, J.B. Fowlkes, C.A. Cain, A new strategy to enhance cavitational tissue erosion using a high-intensity, Initiating sequence, IEEE Trans Ultrason Ferroelectr Freq Control, 53 (2006) 1412-1424.

[20] Z. Xu, J.B. Fowlkes, E.D. Rothman, A.M. Levin, C.A. Cain, Controlled ultrasound tissue erosion: the role of dynamic interaction between insonation and microbubble activity, J Acoust Soc Am, 117 (2005) 424-435.

[21] A.D. Maxwell, C.A. Cain, T.L. Hall, J.B. Fowlkes, Z. Xu, Probability of cavitation for single ultrasound pulses applied to tissues and tissue-mimicking materials, Ultrasound Med Biol, 39 (2013) 449-465.
[22] E. Vlaisavljevich, A. Maxwell, M. Warnez, E. Johnsen, C.A. Cain, Z. Xu, Histotripsy-induced cavitation cloud initiation thresholds in tissues of different mechanical properties, IEEE Trans Ultrason Ferroelectr Freq Control, 61 (2014) 341-352.
[23] E. Vlaisavljevich, Y.Y. Durmaz, A. Maxwell, M. Elsayed, Z. Xu, Nanodroplet-mediated histotripsy for image-guided targeted ultrasound cell ablation, Theranostics, 3 (2013) 851-864.
[24] D. Bartczak, A.G. Kanaras, Preparation of peptide-functionalized gold nanoparticles using one pot EDC/sulfo-NHS coupling, Langmuir, 27 (2011) 10119-10123.
[25] K. Nam, T. Kimura, A. Kishida, Controlling coupling reaction of EDC and NHS for preparation of collagen gels using ethanol/water co-solvents, Macromol Biosci, 8 (2008) 32-37.
[26] L. Wildling, B. Unterauer, R. Zhu, A. Rupprecht, T. Haselgrubler, C. Rankl, A. Ebner, D. Vater, P. Pollheimer, E.E. Pohl, P. Hinterdorfer, H.J. Gruber, Linking of sensor molecules with amino groups to amino-functionalized AFM tips, Bioconjug Chem, 22 (2011) 1239-1248.
[27] R.E. Apfel, C.K. Holland, Gauging the likelihood of cavitation from short-pulse, low-duty cycle diagnostic ultrasound, Ultrasound Med Biol, 17 (1991) 179-185.
[28] E.L. Carstensen, S. Gracewski, D. Dalecki, The search for cavitation in vivo, Ultrasound Med Biol, 26 (2000) 1377-1385.
[29] V. Normand, D.L. Lootens, E. Amici, K.P. Plucknett, P. Aymard, New insight into agarose gel mechanical properties, Biomacromolecules, 1 (2000) 730-738.
[30] R. Masuzaki, R. Tateishi, H. Yoshida, T. Sato, T. Ohki, T. Goto, S. Sato, Y. Sugioka, H. Ikeda, S. Shiina, T. Kawabe, M. Omata, Assessing liver tumor stiffness by transient elastography, Hepatol Int, 1 (2007) 394-397.
[31] J.E. Parsons, C.A. Cain, J.B. Fowlkes, Cost-effective assembly of a basic fiber-optic hydrophone for measurement of high-amplitude therapeutic ultrasound fields, J Acoust Soc Am, 119 (2006) 1432-1440.
[32] E. Herbert, S. Balibar, F. Caupin, Cavitation pressure in water, Physical Review E, 74 (2006).
[33] R.A. Roy, S.I. Madanshetty, R.E. Apfel, An Acoustic Backscattering Technique for the Detection of Transient Cavitation Produced by Microsecond Pulses of Ultrasound, Journal of the Acoustical Society of America, 87 (1990) 2451-2458.
[34] K.W. Lin, Y. Kim, A.D. Maxwell, T.Y. Wang, T.L. Hall, Z. Xu, J.B. Fowlkes, C.A. Cain, Histotripsy beyond the intrinsic cavitation threshold using very short ultrasound pulses: microtripsy, IEEE Trans Ultrason Ferroelectr Freq Control, 61 (2014) 251-265.
[35] T.G. Leighton, The acoustic bubble, Academic Press, San Diego, 1994.